

Formation of $60^\circ \langle 01\bar{1}0 \rangle$ boundaries between $\{10\bar{1}2\}$ twin variants in deformation of a magnesium alloy

Peng Chen^{a,b}, Fangxi Wang^{a,b}, Jamie Ombogo^{a,b}, Bin Li^{a,b,*}

^a Department of Chemical and Materials Engineering, University of Nevada, Reno, USA

^b Nevada Institute for Sustainability, University of Nevada, Reno, USA



ARTICLE INFO

Keywords:

Magnesium
Twinning
Twin-twin interaction

ABSTRACT

Interrupted tensile testing along the normal direction of a rolled AZ31 magnesium plate was conducted at various strain levels from 6% to 15.5%. Prior to deformation the specimens were annealed for grains to coarsen such that multiple twin variants in one grain can be activated and interaction between variants can be better resolved. The grain structure and texture evolution were then examined via electron backscatter diffraction. The results reveal that multiple primary $\{10\bar{1}2\}_p$ twin variants inside individual grains grow and impinge, forming profuse boundaries of $60^\circ \langle 01\bar{1}0 \rangle$ orientation relationship. These boundaries are close to $\{11\bar{2}2\} \langle 11\bar{2}3 \rangle$ twin relationship, however, they are not formed by twin nucleation and are only a product of interaction between the primary twins. The morphology of these special boundaries are highly irregular. Atomistic simulations were performed to understand such interaction, and the results show that such $60^\circ \langle 01\bar{1}0 \rangle$ boundaries have limited mobility. Thus, a primary twin variant is able to grow at the expense of other primary twin variants. Our experimental results also show that $\{10\bar{1}2\}$ twinning is active throughout the deformation until the specimens are fractured. As the strain increases, secondary $\{10\bar{1}2\}_s$ twins are activated inside the primary twins. As the strain further increases to near fracture, $\{10\bar{1}1\}_s$ secondary twins are activated inside the primary twins, followed by activation of tertiary $\{10\bar{1}2\}_t$ twins inside the $\{10\bar{1}1\}_s$ secondary twins, a process known as $\{10\bar{1}1\} - \{10\bar{1}2\}$ double twinning. The formation of irregular $60^\circ \langle 01\bar{1}0 \rangle$ boundaries and the sequential twinning at large strains shed new light on the twinning mechanism in Mg and other hexagonal close-packed metals.

1. Introduction

Deformation twinning plays a crucial role in mechanical properties of hexagonal close-packed (HCP) magnesium (Mg) and its alloys that are the lightest structural metals and have received tremendous attention in recent years [1–4]. Wrought Mg alloys present strong basal texture in which the grains are oriented such that the basal planes are perpendicular to the normal direction (ND) of the rolled sheet/plate, or parallel to the extrusion direction (ED) of the extrudate. When loaded along the direction parallel to the basal planes, Mg presents tension-compression asymmetric yielding [5–7], because deformation twinning is activated when a tensile load is applied along the *c*-axis or a compressive load is applied perpendicular to the *c*-axis of individual crystals. In these cases, the stress-strain curves show typically an S-shape that consists of a low stress stage followed by a stage with a drastically increased hardening rate, and a final, relatively high stress stage in which non-basal dislocation slip dominates the deformation [8–10].

Multiple twinning modes can be activated in deformation of HCP metals. For Mg, the reported twinning modes include $\{10\bar{1}2\}$ extension

twinning, $\{10\bar{1}1\}$ and $\{10\bar{1}3\}$ contraction twinning [11–13], $\{11\bar{2}1\}$ twinning [14,15], as well as “double twinning”, i.e. $\{10\bar{1}1\} - \{10\bar{1}2\}$, $\{10\bar{1}3\} - \{10\bar{1}2\}$ and $\{10\bar{1}2\} - \{10\bar{1}2\}$ twinning modes [16–19]. The most common twinning system is $\{10\bar{1}2\} \langle 10\bar{1}1 \rangle$ which is called “extension twinning”. Extensive experimental observations have shown that this twinning mode presents a wide range of anomalous properties entirely departing from classical twinning [20–22]. When $\{10\bar{1}2\}$ twinning is activated, the parent lattice is reoriented theoretically by 86.3° , but experimental observations revealed that the misorientation angle does not have a unique value and varies around 90° [22].

Multiple $\{10\bar{1}2\}$ twin variants can be activated in a grain. For Mg, Nave and Barnett [23] classified the misorientation relationship into three types: $7.4^\circ \langle 11\bar{2}0 \rangle$ (this relationship was called “co-zone” twin variants by Yu et al. [24] because the variants share the same zone axis $\langle 11\bar{2}0 \rangle$), $60^\circ \langle 01\bar{1}0 \rangle$ and $60.4^\circ \langle 1780 \rangle$ [25]. It should be noted that the misorientation angles in these relationships are only theoretical values. As stated above, the actual misorientation angles can appreciably deviate from these values due to the non-classical characteristics of this particular twinning mode [22]. When different variants impinge,

* Corresponding author.

E-mail address: binl@unr.edu (B. Li).

<https://doi.org/10.1016/j.msea.2018.10.029>

Received 22 August 2018; Received in revised form 4 October 2018; Accepted 5 October 2018

Available online 12 October 2018

0921-5093/© 2018 Elsevier B.V. All rights reserved.

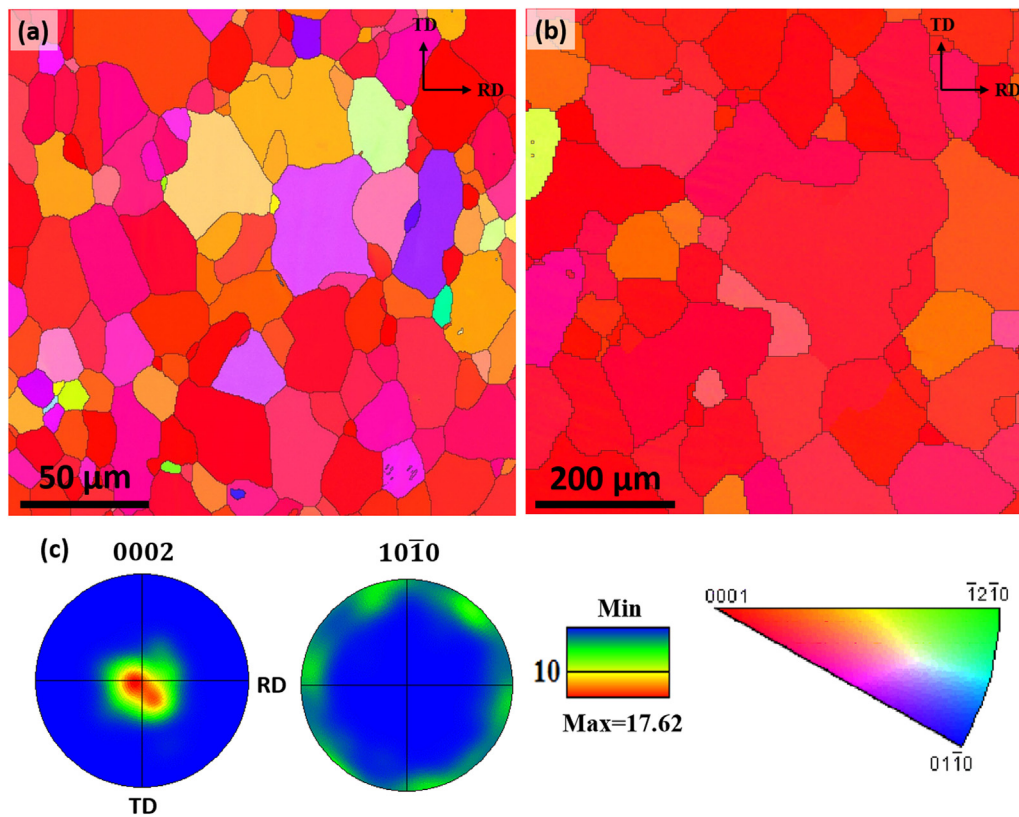


Fig. 1. Initial texture and grain structure of (a) as-rolled AZ31 alloy; (b) After annealing at 500 °C for 24 h; (c) Pole figure of the TD of the specimen after annealing.

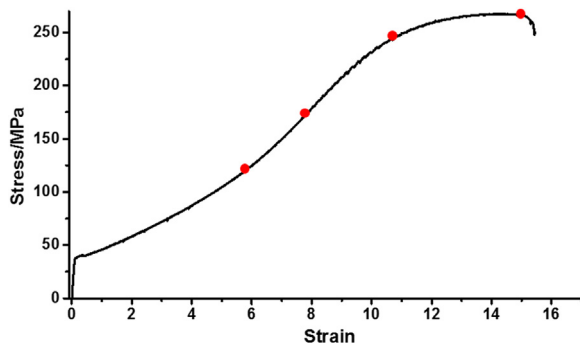


Fig. 2. Stress-strain curve under monotonic tension along the normal direction (ND) of the AZ31B rolled plate after annealing. The red dots denote the strain levels at which the tension test was interrupted for EBSD analysis.

interaction between variants ensues. Twins of the same variant in a grain can merge when the twin boundaries meet. But twins of different variants interact when they impinge and the growth of the impinging variants slows down [26]. Yu et al. [24] studied co-zone twin-twin interaction in a Mg single crystal. It was shown that one variant does not transmit across the twin boundary of the other. But when two variants with different zone axis interact, one variant may transmit into the other under some special loading [25]. In contrast, Morrow et al. [27] observed that twin-twin interaction may accelerate the motion of the twin-twin interface by using in-situ transmission electron microscopy (TEM).

Most recently, the $60^\circ \langle 01\bar{1}0 \rangle$ boundaries between twin variants were reported in deformed Mg by a number of researchers [28–33]. Mokdad et al. [14] reported that the co-zone twin-twin interaction results in ladder-like twinning structure while the interaction between the non-co-zone twin variants leads to twin branching. These interactions between different variants were also observed and analyzed by Hong

et al. [34] and they suggested the nucleation of twin variants is governed by the Schmid law. It is worth noting that crystallographically, the misorientation relationship of this type of boundaries is very close to $\{11\bar{2}\}\langle 11\bar{2}\bar{3} \rangle$ twinning ($58.4^\circ \langle 01\bar{1}0 \rangle$) that has been observed only in HCP metals such as titanium and zirconium but not in Mg [35–37]. Most of these previous reports were conducted at low strain levels.

To better understand the interaction between different twin variants, this work investigates the twinning behavior at high strain levels up to fracture, with a focus on the formation and evolution of the $60^\circ \langle 01\bar{1}0 \rangle$ boundaries between twin variants during plastic deformation of a Mg alloy with a relatively large grain size which enables nucleation of multiple twin variants inside individual grains and interaction between them. The results obtained shed new light on deformation behavior of wrought Mg alloys.

2. Methods

The 76 mm thick (~ 3.0 in.), commercial hot-rolled AZ31B Mg plate (Metalmart International, Inc.) with a chemical composition (wt%) of 2.60Al-0.9Zn-0.37Mn (Mg the balance) was used in this study. The AZ31B samples were annealed in a tube furnace at 500 °C for 24 h in an inert argon atmosphere followed by immediate water quenching. Specimens for tensile tests were then machined, with a gauge length of 25 mm, a thickness of 4 mm and a width of 6 mm. The longitudinal direction of the dog-bone specimens is along the normal direction (ND) of the rolled plate. An Instron load frame with a loading capacity of 25 kN was used to conduct the tensile tests, which were carried out in strain-control mode at a strain rate of 10^{-4} /s at ambient temperature. The specimens were deformed to four strain levels: 6%, 8%, 11% and 15.5% (fracture). Samples for electron backscatter diffraction (EBSD) scans were cut from the tensioned specimens and the sample surface perpendicular to the loading direction was prepared for EBSD scans. The samples were ground mechanically down to 1200/4000 grit number on SiC sand papers, followed by electrochemical polishing with

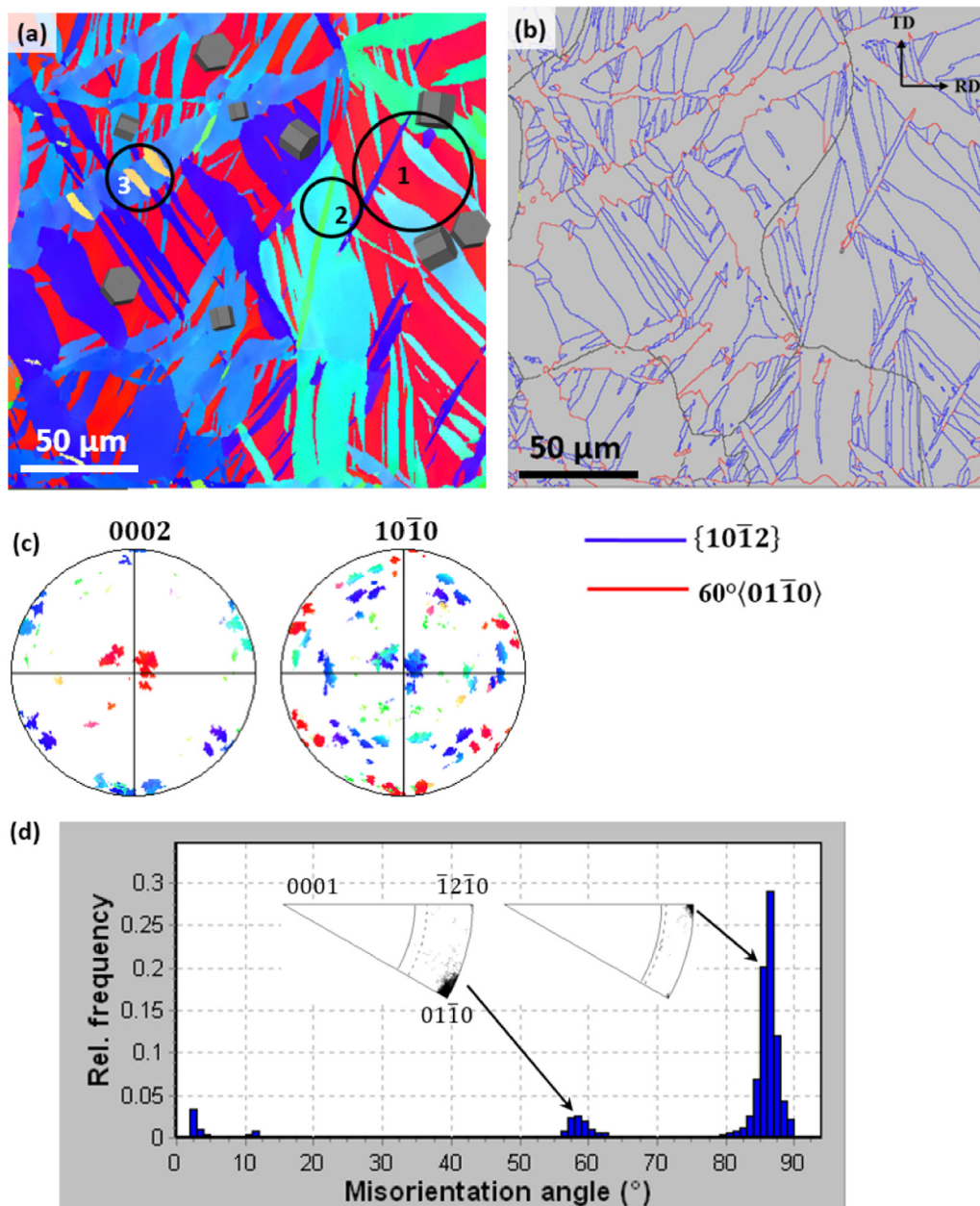


Fig. 3. EBSD analysis of the annealed specimen at the strain of 6%. (a) IPF map. The parent (in red) is being consumed by extension twin variants. (b) Band contrast map. (c) Pole figures. (d) Misorientation angle distribution. High density $\{10\bar{1}2\}$ twin boundaries with a misorientation angle of $\sim 86^\circ$ are observed. A small peak around 60° with zone axis $\langle 01\bar{1}0 \rangle$ can also be seen, corresponding to the red boundaries in (b). (For interpretation of the references to colour in this figure legend, the reader is referred to the web version of this article.)

a solution of 5% nitric acid, 0.5% perchloric acid and 94.5% ethanol at 20 V for ~ 20 s. EBSD scans were conducted on a JEOL 7100F field emission scanning electron microscope (SEM) with an Oxford HKL Channel 5 instrument. An acceleration voltage of 20 kV, a working distance of 25 mm, and a step size of 0.5–1.0 μm were used.

To further investigate the mechanism of interaction between twin variants, atomistic simulations were also conducted. The embedded atom method (EAM) [38,39] potential for Mg–Al binary system was used. This EAM potential was well developed by Liu et al. [40] and has been used in numerous atomistic simulations of Mg and Mg alloys [12,41]. A single crystal was first constructed with a dimension of $57 \times 33 \times 26 \text{ nm}^3$, containing a total number of atoms about 2.12 million. The system was relaxed before an external tensile strain was applied along the c -axis of the crystal. Free surfaces were applied to all three dimensions. The tensile strain was generated by moving the atoms

on the left surface layer at a constant displacement rate of 0.01 nm per femtosecond, corresponding to a strain rate of $1.7 \times 10^{11}/\text{s}$ which is typical for atomistic simulations. The temperature was maintained at 100 K during simulation.

3. Results

3.1. Experimental observations

The initial grain structure of the as-rolled AZ31 plate is shown in the inverse pole figure (IPF) map (Fig. 1a). After annealing, the average grain size increases from $\sim 35 \mu\text{m}$ to $\sim 120 \mu\text{m}$ (Fig. 1b). As shown in Fig. 1c, the annealed specimen displays a typical basal texture with the basal pole of most grains orientated around the ND.

The stress–strain curve under monotonic tension along the normal

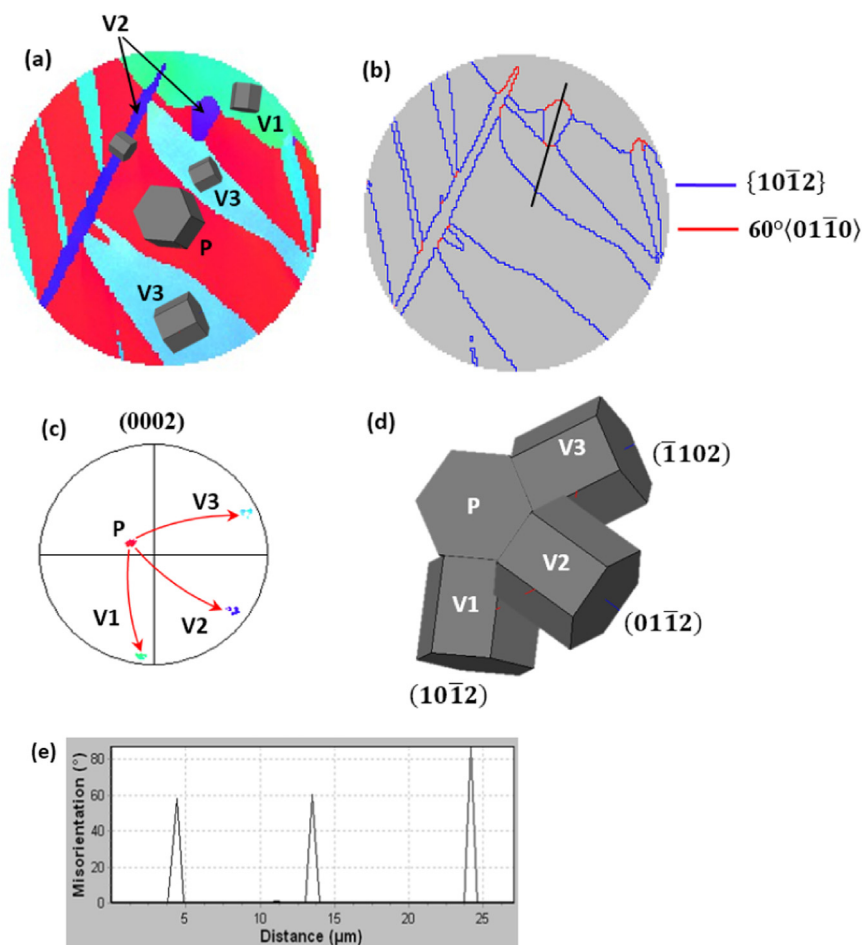


Fig. 4. $\{10\bar{1}2\}$ twin variants analysis in the circled region 1 in Fig. 3a. (a) Three variants V1, V2 and V3 can be observed. (b) Band contrast map. The misorientation angle along the black line are measured. (c) Pole figure showing how the parent is transformed to the three variants. (d) Unit cells for the parent, V1, V2 and V3 primary twin variants. The misorientation between the neighboring twin variants satisfies $60^\circ \langle 01\bar{1}0 \rangle$. (e) Misorientation angles measured in (b). (For interpretation of the references to colour in this figure legend, the reader is referred to the web version of this article.)

direction (ND) of the rolled plate after annealing is shown in Fig. 2. The deformation behavior presents an S-shaped curve which is typical of wrought Mg alloys with a strong basal texture. The tensile tests were interrupted at four strain levels: $\epsilon = 6\%$, 8% , 11% and 15.5% , which are denoted by the red dots on the stress-strain curve. Then the specimens were examined with EBSD.

The IPF map of the annealed specimen at the strain of 6% is shown in Fig. 3a. The red patches are the parent crystals that are being consumed by the primary $\{10\bar{1}2\} \langle 10\bar{1}1 \rangle$ extension twins which are displayed in dark blue, light blue, cyan and green. From the hexagonal units that are superimposed on the twin variants, we can see that at least five different twin variants have been activated inside the parent grains. To identify the types of the boundaries in terms of misorientation and rotation axis, band contrast map is plotted in Fig. 3b. The $\{10\bar{1}2\}$ extension twin boundaries are marked in blue. Another type of boundaries are plotted in red, satisfying $60 \pm 5^\circ$ misorientation with a rotation axis $\langle 01\bar{1}0 \rangle$. Fig. 3c shows the pole figure (PF) of Fig. 3a. If we compare this pole figure with the original before tensile deformation (Fig. 1c), it can be seen that, actually all the possible $\{10\bar{1}2\}$ twin variants have been activated (the discrete spots around the big circle on the 0002 pole). Fig. 3d shows the misorientation angle distribution. The outstanding peak near 90° misorientation corresponds to the $\{10\bar{1}2\}$ twin boundaries, most of which are between the primary $\{10\bar{1}2\}$ twins and the parent crystals. Also can be seen is the peak near 60° and these boundaries correspond to the red boundaries in Fig. 3b, which has a rotation axis of $\langle 01\bar{1}0 \rangle$.

In Fig. 3a, three regions, denoted by the black circles 1, 2 and 3, are

selected for further EBSD analysis of twin variants. Fig. 4a shows $\{10\bar{1}2\}$ twin variants in region 1. Three $\{10\bar{1}2\}$ twin variants, V1 ($10\bar{1}2$) (in green), V2 ($01\bar{1}2$) (in dark blue), V3 ($\bar{1}102$) (in cyan) can be observed. It can be seen that the V2 needle impinges into V1. Two kinds of boundaries can now be better resolved in the band contrast map (Fig. 4b): the blue $\{10\bar{1}2\}$ boundaries of the primary twins, and the red boundaries where the primary twins impinge. The (0002) pole figure of the parent crystal and the twin variants are shown in Fig. 4c. We can see that the parent is transformed to three twin variants, each of which is reoriented by $\sim 90^\circ$ with respect to the parent with a zone axis of $\langle 11\bar{2}0 \rangle$. To better reveal the misorientation relationship, 3D hexagonal lattice units for the parent, V1, V2 and V3 primary twin variants are plotted in Fig. 4d. The misorientation relationship between the neighboring twin variants satisfies $60^\circ \langle 01\bar{1}0 \rangle$, and the corresponding misorientation angle between basal planes of the twin variants are 120° . Point-to-point misorientation angles along the black line in Fig. 4b are measured and plotted in Fig. 4e. It can be clearly seen that the interface between two impinging twin variants has a misorientation angle close to 60° .

In addition to $\{10\bar{1}2\}$ primary twins that are activated in the parent grains, secondary $\{10\bar{1}2\}$ twins are also activated inside the primary twins, as shown in Fig. 5a and b, which are the circled region 2 and 3 in Fig. 3a, respectively. In these two scenarios, secondary $\{10\bar{1}2\}$ twinning is activated despite the stress condition strongly disfavors the secondary twins. It can also be seen that at this strain level ($\epsilon = 6\%$), the density of the secondary twins is not high. Thus, $\{10\bar{1}2\}$ primary twinning dominates the plastic deformation, as reported by Chen et al. [42]. The pole

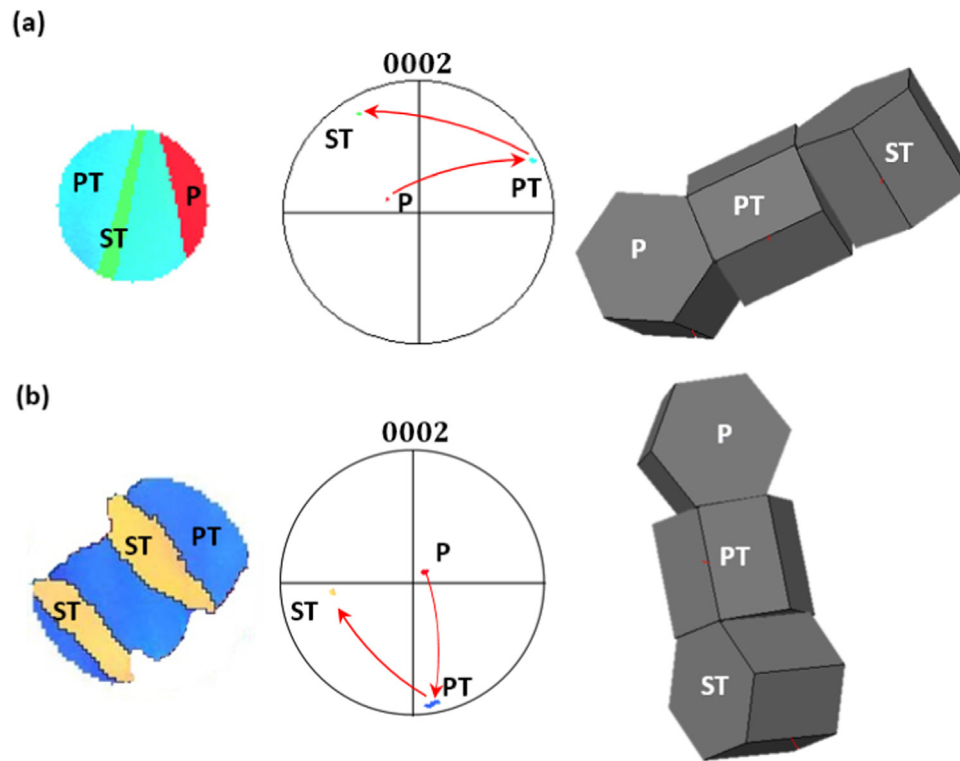


Fig. 5. $\{10\bar{1}2\}$ twin variant analysis in the circled region 2 and 3 in Fig. 3a. (a) The cyan is a primary twin (PT) and the light green is a secondary twin (ST) which is formed inside the PT. (b) A primary twin (in blue) and two secondary twins (in brown) that are formed inside the PT. (For interpretation of the references to colour in this figure legend, the reader is referred to the web version of this article.)

figures and the hexagonal lattice units clearly show the sequence of twinning. If we compare the band contrast map with the IPF map in Fig. 3, it can be readily seen that the red boundaries also include the boundaries between the parent and the secondary variants. The misorientation angle between parent and the secondary twins is also $\sim 60^\circ$ with a zone axis of $\langle 01\bar{1}0 \rangle$. However, because the secondary twins are only formed inside the primary twins, and the parent grains are being consumed by the primary twins, few $60^\circ \langle 01\bar{1}0 \rangle$ boundaries are formed between the parent crystals and the secondary $\{10\bar{1}2\}$ twins.

Further increase in strain leads to increase of twin volume fraction as the primary twins grow thicker, impinge and eventually coalesce. As the strain was increased to 8%, most of the parent grains are consumed by $\{10\bar{1}2\}$ primary twinning, as shown in Fig. 6a. Only small patches of parent grains (in red) can be seen at this strain level. Three primary twins, i.e. PT1, PT2 and PT3, can be identified from the hexagonal lattice units that are superimposed on the crystals. As denoted by the black arrows, small, lenticular-shaped PT2 pieces (in dark blue) are surrounded by the PT1 (in light blue). Concomitant with the interaction between the primary twins, more $\{10\bar{1}2\}$ secondary twins (in green and in white) are activated inside the primary twins, as indicated by the white arrows. As a result of the interaction between the primary twins, the density of $60^\circ \langle 01\bar{1}0 \rangle$ boundaries increases, as shown in the band contrast map (Fig. 6b), compared with Fig. 3b. In the pole figure (Fig. 6c), more and more spots appear near the big circle of the (0002) pole due to the primary twins. Spots of secondary twinning can also be seen. Fig. 6d shows the misorientation angle distribution at the strain of 8%. Clearly, the intensity of the peak near 60° significantly increases if compared with Fig. 3d.

As the strain increases to 11%, nearly all the parent grains have been twinned, as shown in Fig. 7a. Small patches in red are the leftover of parent grains that have largely been consumed by the primary twins. At this strain level, the primary twinning has been saturated. Meanwhile, a rather high density of $\{10\bar{1}2\}$ secondary twins are formed inside the primary twins, as indicated by the black and white arrows. The

interaction between the primary twins and the formation of secondary twins can be better viewed in the band contrast map (Fig. 7b). The red lines unambiguously delineate the boundaries between the primary twins, and the blue lines denote the $\{10\bar{1}2\}$ boundaries between the primary and secondary twins. An important feature in Fig. 7a and b is that the $60^\circ \langle 01\bar{1}0 \rangle$ boundaries are highly irregular. The pole figure (Fig. 7c) shows that the parent grains are nearly totally twinned, and clustered spots with high intensities appear around the big circle of the (0002) pole. The misorientation angle distribution (Fig. 7d) displays a high peak around 90° , which mainly comes from the secondary twins inside the primary twins. The intensity of $60^\circ \langle 01\bar{1}0 \rangle$ boundaries further increases with increasing strain.

The boxed region in Fig. 7a is further analyzed in Fig. 8 to better understand the highly irregular $60^\circ \langle 01\bar{1}0 \rangle$ boundaries. As shown in Fig. 8a, three primary twin variants PT1, PT2 and PT3 are activated. Secondary twins ST1 are formed inside the primary twin PT1, and another secondary twin ST2 is formed inside PT2. The pole figure in Fig. 8b shows the parent is transformed to the three primary twin variants by a rotation of $\sim 90^\circ$ around the $\langle 11\bar{2}0 \rangle$ zone axis. From the band contrast map in Fig. 8c, it can be found that the boundaries in red, i.e. $60^\circ \langle 01\bar{1}0 \rangle$ boundaries, are a result of the interactions between primary twins. These boundaries are highly irregular, suggesting strong interaction between twin variants. The boundaries in blue are either the interface between primary twin and the parent or the interface between secondary twin and primary twin.

As the tensile strain was increased to the level of fracture ($\sim 15.5\%$), the parent grains are totally twinned, as shown in Fig. 9a–c. The scanned region is near the fracture surface. Twin-like, lenticular domains, alternating in purple and in cyan, can be observed in the interior of the twinned grains. These domains are $60^\circ \langle 01\bar{1}0 \rangle$ boundaries between the primary twins, as seen in the band contrast map (Fig. 9b), and these boundaries are rather profuse inside the parent grains. From Fig. 9b, inside the twinned grains, $60^\circ \langle 01\bar{1}0 \rangle$ boundaries are predominant. Aside from the lenticular morphology, there are also 60°

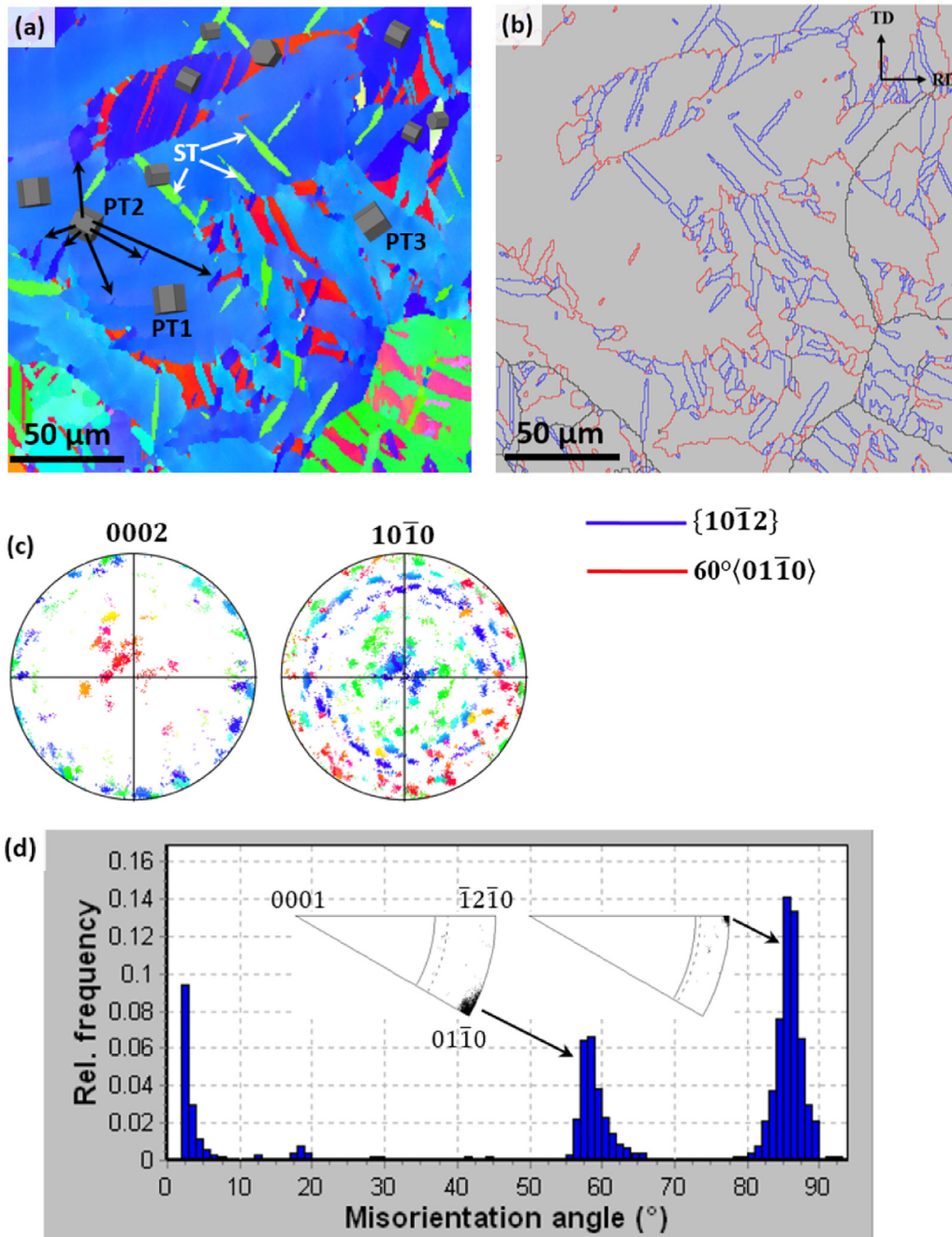


Fig. 6. EBSD analysis of twin variants in the annealed specimen as the strain was increased to 8%. (a) IPF map. (b) Band contrast map. The red boundaries are 60° $\langle 01\bar{1}0 \rangle$ type. (c) Pole figures. (d) Misorientation angle distribution. Note the density of 60° $\langle 01\bar{1}0 \rangle$ boundaries increases with increasing strain. (For interpretation of the references to colour in this figure legend, the reader is referred to the web version of this article.)

$\langle 01\bar{1}0 \rangle$ boundaries that appear to be highly irregular. Notably, at this strain to failure, $\{10\bar{1}1\}-\{10\bar{1}2\}$ double twins can now be observed. The boundaries of these double twins are plotted in cyan, which satisfy $38 \pm 5^\circ \langle 11\bar{2}0 \rangle$ misorientation relationship. As shown in the misorientation angle distribution (Fig. 9d), the intensity of 60° $\langle 01\bar{1}0 \rangle$ boundaries decreases. Still a small peak near 90° can be seen due to secondary twinning that occurs inside the primary twins. A new peak around 40° appears, corresponding to $\{10\bar{1}1\}-\{10\bar{1}2\}$ double twinning. However, these double twins are formed inside the primary $\{10\bar{1}2\}$ twins. Thus, the actual twinning sequence from the beginning of plastic deformation should be as following: first, primary $\{10\bar{1}2\}$ twins are activated in the parent grains, then secondary $\{10\bar{1}1\}$ contraction twins are activated inside the primary $\{10\bar{1}2\}$ twins, then tertiary $\{10\bar{1}2\}$ twins are

activated inside the $\{10\bar{1}1\}$ secondary twins, i.e. $\{10\bar{1}2\}_p - \{10\bar{1}1\}_s - \{10\bar{1}2\}_t$ triple twinning.

Analyses of the twin variants in the circled region 1 and 2 in Fig. 9a are shown in Figs. 10 and 11, respectively. The variants of secondary $\{10\bar{1}2\}$ twinning can form 60° $\langle 01\bar{1}0 \rangle$ boundaries as well, as shown in Fig. 10a–e. Two secondary twins that are nucleated inside the primary twin grow and impinge, forming the red boundary in Fig. 10b. The pole figure (Fig. 10c) and the unit cells of the twin variants (Fig. 10d) clearly show the misorientation relationship between the twin variants. The misorientation angles along the black line in Fig. 10b are ~ 60° and ~ 90°, corresponding to the red boundary between the two secondary twin variants and the blue boundaries between the primary and the secondary twins. One example of the crystallographic relationship in

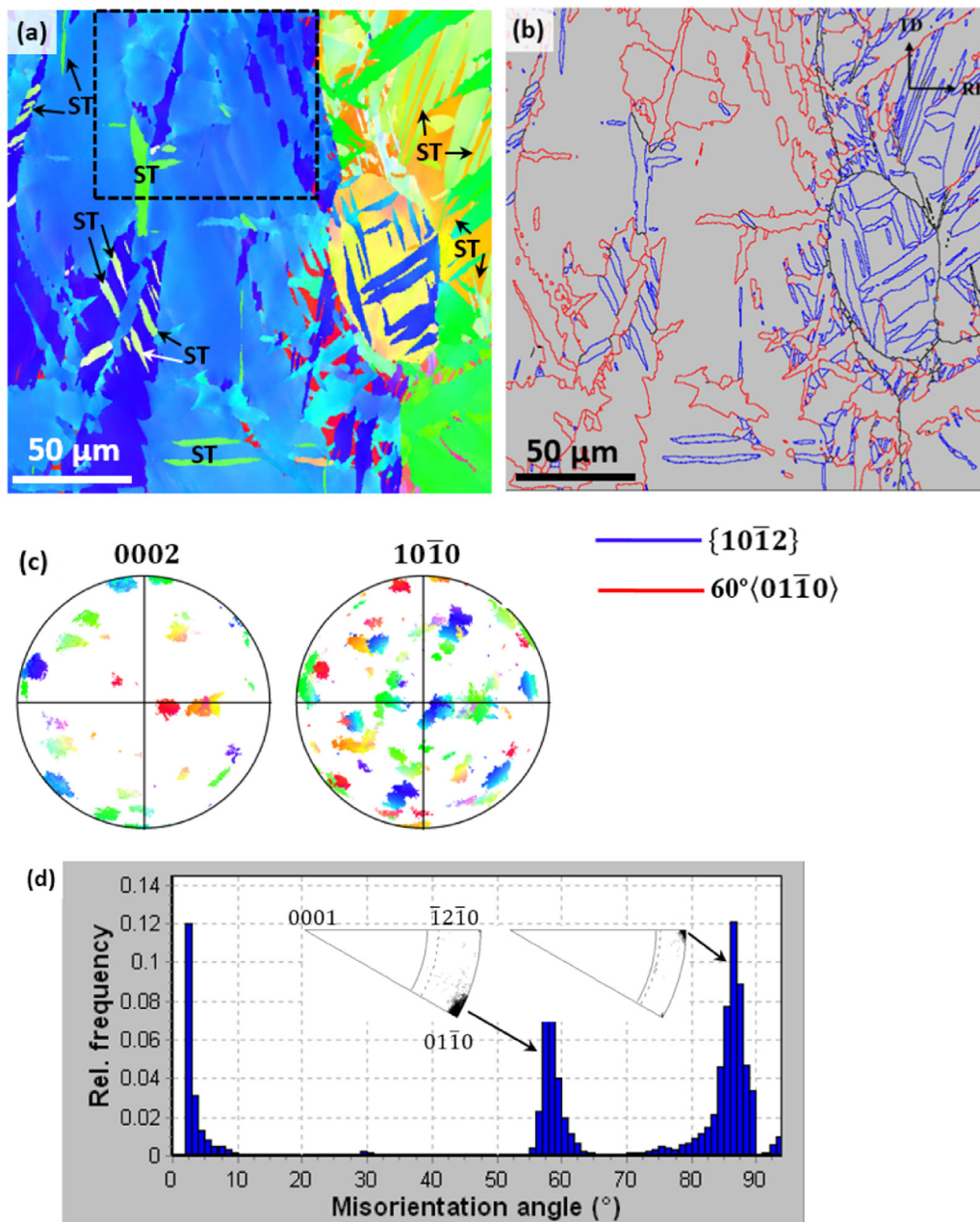


Fig. 7. EBSD analysis of twin variants in the annealed specimen as the strain was increased to 11%. (a) IPF map. The red patches are leftover of the parent that has not twinned. (b) Band contrast map. (c) Pole figures. (d) Misorientation angle distribution. The peak around 90° mainly comes from the secondary twins inside the primary twins. (For interpretation of the references to colour in this figure legend, the reader is referred to the web version of this article.)

the $\{10\bar{1}2\}_P - \{10\bar{1}1\}_S - \{10\bar{1}2\}_T$ triple twinning is shown in Fig. 11a–c. The $\{10\bar{1}1\}$ secondary twin inside the primary twin has been transformed to the $\{10\bar{1}2\}$ tertiary twin.

3.2. Simulation results

In the following, we show simulation results to better understand the interaction between $\{10\bar{1}2\}$ twin variants on the atomistic level. $\{10\bar{1}2\}$ twin nucleation and interaction between variants are shown in Fig. 12a–f, in time sequence. Fig. 12a shows a snapshot of the Mg single crystal before twin nucleation is activated. Only a portion of the system is displayed. As the tensile strain increases, multiple twin variants are activated (Fig. 12b). In these plots, common neighbor analysis (CNA) [43,44] was used to display the structures inside the system. For instance, the HCP structure is plotted in red; FCC in green (the basal

stacking faults inside the twins); and atoms on the surfaces and boundaries in white. We denote two primary $\{10\bar{1}2\}$ twins as Variant 1 and 2 which nucleate and grow inside the parent (Fig. 12b), and focus on the interaction between these two variants. As the tensile strain further increases, Variant 1 grows into Variant 2 and expands at the expense of Variant 2 (Fig. 12c and d). As the straining continues (Fig. 12e and f), the portion of Variant 2 in the upper right corner is almost consumed by Variant 1. While Variant 2 grows toward the left, Variant 1 further expands and consumes Variant 1, as indicated by the yellow arrows.

The orientation relationship between Variant 1 and 2 is analyzed in Figs. 13 and 14. Fig. 13a shows a magnified view of the interfacial region of Variant 1 and 2. The basal plane of Variant 2 is perpendicular to the figure plane. Then, the slice is rotated around the $[0002]$ of the parent by $\sim 60^\circ$, such that the basal plane of Variant 1 is perpendicular

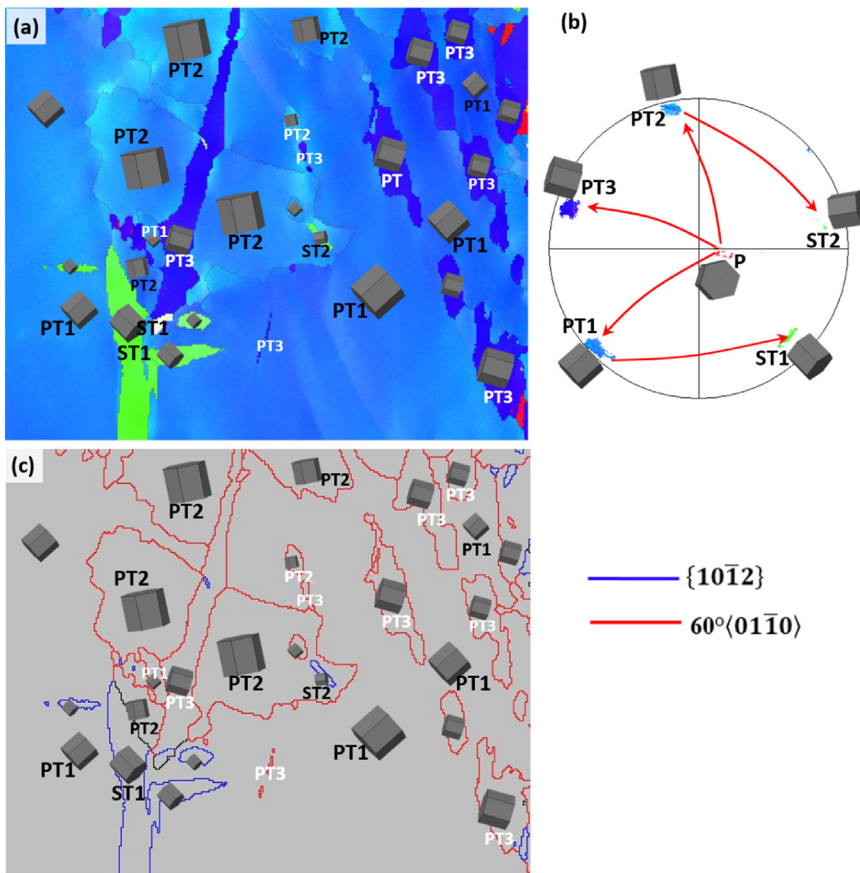


Fig. 8. Twin orientation analysis in the boxed region in Fig. 7a. (a) Three primary twin variants PT1, PT2 and PT3 are observed. Secondary twins ST1 are formed inside PT1, and another secondary twin ST2 is formed inside PT2. The 3-D unit cells are superimposed to show the orientation relationship between the different variants. (b) Pole figure showing how the parent is transformed to the three primary twins and how the primary twins are transformed to secondary twins. (c) Band contrast map. The boundaries in red are a result from the interaction between primary twins, these boundaries are highly irregular. (For interpretation of the references to colour in this figure legend, the reader is referred to the web version of this article.)

to the figure plane (Fig. 13b). Clearly, the boundary between Variant 1 and 2 in Fig. 13a is a twist boundary and mobile in our simulations. A side view of the boxed region in Fig. 13b is shown in Fig. 14. The zone axis of Variant 1 and 2 can be readily identified as $\langle 1\bar{1}00\rangle$, and the angle between the basal planes of the two variants is $\sim 60^\circ$. Thus, the boundaries between the twin variants are all $60^\circ\langle 01\bar{1}0\rangle$ type, which is consistent with our experimental results.

Our atomistic simulations show that $60^\circ\langle 01\bar{1}0\rangle$ boundaries between $\{10\bar{1}2\}$ twin variants have limited mobility under external strain, especially at large strains close to fracture.

4. Discussion

4.1. Contribution of sequential twinning to deformation

With the heat treated AZ31 specimens that have relatively large grain size, and the interrupted tensile testing, we reveal a sequence of twinning activities with a much clearer picture. It should be pointed out that similar twinning behavior was also observed in the as-rolled specimens without heat treating. It can be expected that the observed sequence of twinning activities should happen in rolled Mg and Mg alloys with a strong basal texture under tension along the ND. As suggested by the name of “extension twinning”, $\{10\bar{1}2\}$ twinning creates an extension along the c -axis when a single crystal is pulled along the $[0002]$, and a contraction in the direction perpendicular to the $[0002,45]$ when the hexagonal lattice is reoriented by $\sim 90^\circ$ by twinning. This twinning process entirely differs from a shear deformation on an invariant plane, i.e. the twinning plane which is required to be structurally undistorted in the classical twinning theory [46]. According to recent works [28,45] the $\{10\bar{1}2\}$ twinning plane cannot retain invariant during twinning. Thus, the Schmid law, which can only be applied to plastic deformation in which a shear is involved, is not applicable for this particular

twinning mode, as shown in numerous experimental observations of non-Schmid effect [16,47]. Mu et al. [48] reported that the migration of the primary twin is not governed by Schmid law but controlled by strain accommodation, i.e. the variant that requires the least activation of the difficult slip systems in the adjacent grain spreads more extensively than the others. This criterion not only applies to the primary twin, but also works for the secondary and tertiary twin. From the pole figure in Fig. 3c, all the possible $\{10\bar{1}2\}$ twin variants have equal probability to be activated when a specimen is loaded along the ND. As a result, impingement between the twin variants takes place all over the parent grains during deformation.

The stress-strain curve (Fig. 2) looks very similar to that of an extruded specimen when compressed along the extrusion direction (ED) [42]. However, the deformation modes that are activated at different stages can be very different. When compressed along the ED, extension twinning is activated and dominates the low stress stage deformation [42], but often only one most favorable twin variant dominates in a grain in most cases (activation of multiple variants is possible and dependent on the location where a specimen is sampled from the extrudate). Although nucleation of a favorable twin variant can be at multiple locations inside a grain, these twins of the same variant grow and merge when they meet and form a larger twin. Thus, interaction between primary twins is expected to be much less conspicuous in extruded specimens. As shown by [30], $\{10\bar{1}2\}$ secondary twins can also be activated inside the primary twins in an extruded AM30 alloy as strain increases. Although such secondary twins are disfavored by the stress condition, they can still be activated by the fact that two strain components are generated by $\{10\bar{1}2\}$ twinning mode and the contraction component perpendicular to the c -axis may contribute to strain accommodation as well if the stress is sufficiently high [45].

If we compare the IPF maps and the band contrast maps (Figs. 3, 6–9) with the stress-strain curve (Fig. 2), it can be readily seen that in

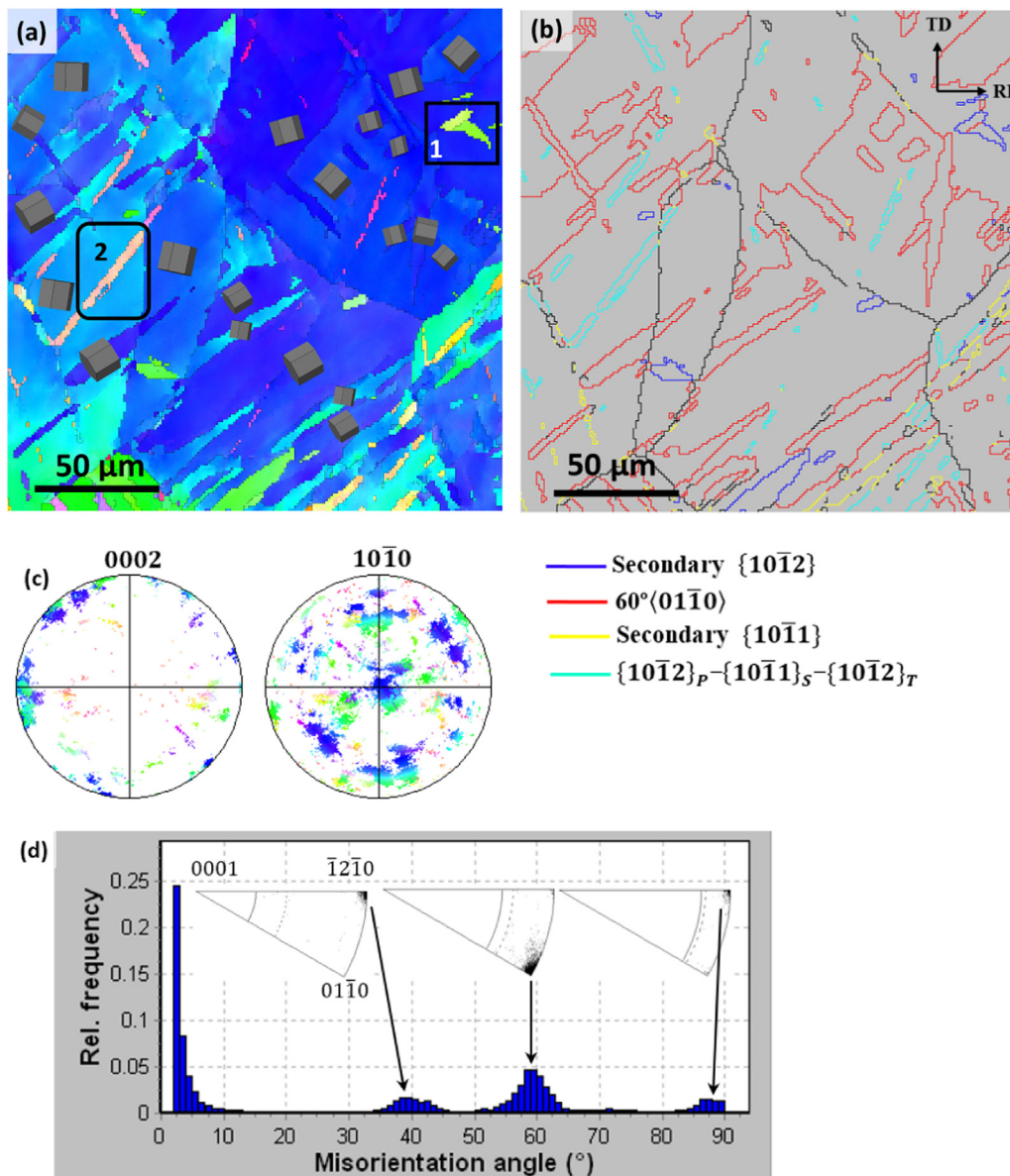


Fig. 9. EBSD analysis of the annealed specimen after fracture ($\sim 15.5\%$ strain). (a) IPF map. The unit cells are superimposed to show the orientation relationship between twin variants. (b) Band contrast map. (c) Pole figures. The specimen is totally twinned. (d) Misorientation angle distribution. The red boundaries in (b) are $60^\circ\langle 01\bar{1}0\rangle$ type. The green boundaries are produced by the following twinning sequence: first, primary $\{10\bar{1}2\}$ twins are activated in the parent grains, then secondary $\{10\bar{1}1\}$ contraction twins are activated inside the primary $\{10\bar{1}2\}$ twins, then tertiary $\{10\bar{1}2\}$ twins are activated inside the $\{10\bar{1}1\}$ secondary twins, i.e. $\{10\bar{1}2\}_P - \{10\bar{1}1\}_S - \{10\bar{1}2\}_T$ triple twinning. (For interpretation of the references to colour in this figure legend, the reader is referred to the web version of this article.)

the rolled specimens, $\{10\bar{1}2\}$ twinning is active until fracture. This is rather different from the current understanding that $\{10\bar{1}2\}$ twinning is mostly activated during the low stress stage deformation and saturates around 6–7% plastic strain. It has been believed that, non-basal dislocation slip systems such as prismatic and pyramidal slips are activated at higher stresses. Because the critical stresses for activating these non-basal slip systems are much higher (a factor of three to two orders of magnitude higher [49]) than that of basal slip, these slip systems significantly contribute to the unusually high hardening rate [5]. Additionally, twin-slip interaction may also contribute to the high hardening rate [50,51]. However, the most recent work by Wu et al. [10] suggested that elastic deformation, which comes from the twinned parent grains, should be counted as an important contributor as well. This premise is plausible because after twinning saturates in extruded Mg specimens, the stress may be lower than the critical stresses for the non-basal slip systems, but the basal slip system is disfavored by the

loading condition. Earlier work by Lou et al. [52] assumed that the S-shaped stress-strain curve (Fig. 2) can be approximately described by two yield surfaces: low stress yielding which is caused by $\{10\bar{1}2\}$ twinning, and high stress yielding which corresponds to activation of non-basal slip. Thus, contribution of non-basal slip and twin-slip interaction to the abnormally high hardening rate may be not as significant as thought before. Most recent study by Chen et al. [53] on the stress-strain behavior of extruded AZ31 shows that indeed, the contribution of twin-slip interaction to hardening is negligible.

In contrast to extruded Mg, the scenario in our rolled specimens is quite different. At the low stress stage, multiple primary twin variants have been activated and interaction between these variants contributes to hardening already. As the primary twinning saturates around 7% strain, the stress is not sufficiently high to activate the non-basal slip systems. The secondary $\{10\bar{1}2\}$ twinning is activated inside the primary twins at this intermediate stress level. Bian et al. [54] found that the

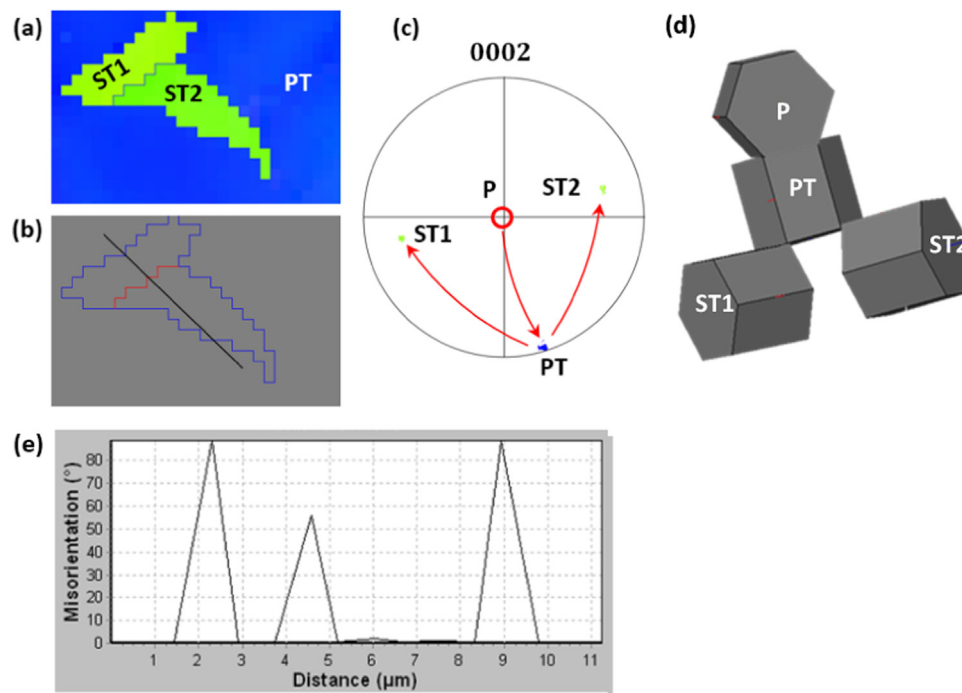


Fig. 10. Misorientation analysis of the circled region 1 in Fig. 9a. (a) Two $\{10\bar{1}2\}$ secondary twins inside a primary twin. (b) The band contrast map. Misorientation angles are measured along the black line. (c) The pole figure. (d) Unit cells of the twin variants. (e) Misorientation angles along the black line in (a). (For interpretation of the references to colour in this figure legend, the reader is referred to the web version of this article.)

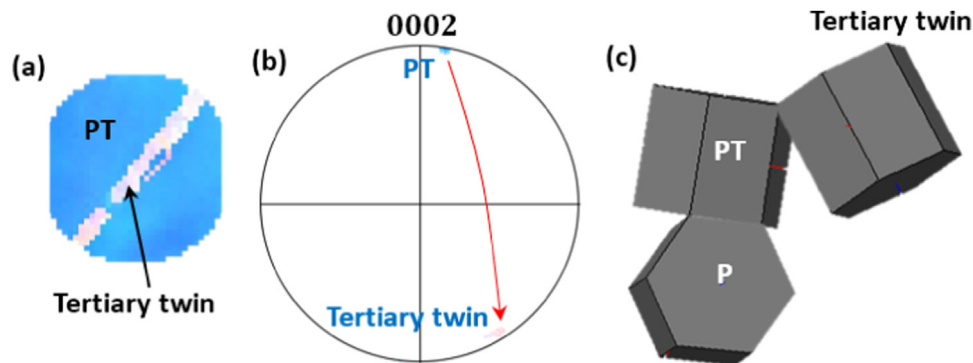


Fig. 11. Misorientation analysis of the circled region 2 in Fig. 9a. (a) $\{10\bar{1}2\}_P - \{10\bar{1}1\}_S - \{10\bar{1}2\}_T$ triple twinning. A $\{10\bar{1}1\} - \{10\bar{1}2\}$ double twin is formed inside of a primary extension twin. (b) Pole figure. (c) Unit cells of the twins.

$\{10\bar{1}2\}$ secondary twin which is formed inside the primary twin has non-Schmid behavior. In our work, the activation of the $\{10\bar{1}2\}$ secondary twinning is probably due to the internal local plastic strain concentration caused by the interaction between $\{10\bar{1}2\}$ primary twins. Jain et al. [55] studied the $\{10\bar{1}2\}$ secondary twinning behavior in an AZ80 alloy at 77 K, they suggested the appearance of the secondary twinning may serve as an accommodation mechanism to maintain strain compatibility and contribute to plastic deformation. Between 8% and 11% strains (Fig. 2), secondary extension twinning continues. Meanwhile, interaction between the primary twins becomes stronger as the primary twins grow, impinge and engulf one another (Figs. 6–7). Moreover, elastic deformation of the twinned parent grains contributes to the overall strain. As a result of the combined effect of these three contributors, the transition from the low stress stage to the high stress flow stage presents a superficially high hardening rate. During the final flow stage, secondary twinning continues but subsides. Non-basal slip systems are activated when the stress is sufficiently high. As the strain increases to near fracture, $\{10\bar{1}1\}$ secondary twins appear inside the $\{10\bar{1}2\}$ primary twins. Then the $\{10\bar{1}1\}$ secondary twins are twinned and transformed into $\{10\bar{1}2\}$ tertiary twins, i.e. $\{10\bar{1}1\} - \{10\bar{1}2\}$ double twinning. The

double twinning transforms the mobile $\{10\bar{1}1\}$ twin boundaries into immobile $38^\circ\langle 11\bar{2}0 \rangle$ boundaries, and this leads to local stress concentration and localized plastic flow at these immobile boundaries, and eventually final fracture ensues [56].

4.2. $60^\circ \langle 01\bar{1}0 \rangle$ boundaries and twin-like domains

In this work, high density $60^\circ \langle 01\bar{1}0 \rangle$ boundaries were first observed in the specimen that was deformed to fracture, i.e. Fig. 9. These boundaries were so intriguing that we initially hypothesized that the lenticular, twin-like domains inside the parent grains were “ $\{11\bar{2}2\}\{11\bar{2}\bar{3}\}$ twins” that have not been observed in Mg. However, after we carefully examined the highly irregular morphology of these boundaries which totally depart from coherent twin boundaries, a question arises as to how these boundaries were generated. This question prompted us to perform the interrupted tensile tests at different strain levels as shown in Fig. 2. Our results clearly indicate that the twin-like domains are formed due to the interaction between $\{10\bar{1}2\}$ primary twin variants. Twin-like domains were reported by Li et al. [57] when an as-cast pure Mg specimen was compressed to failure.

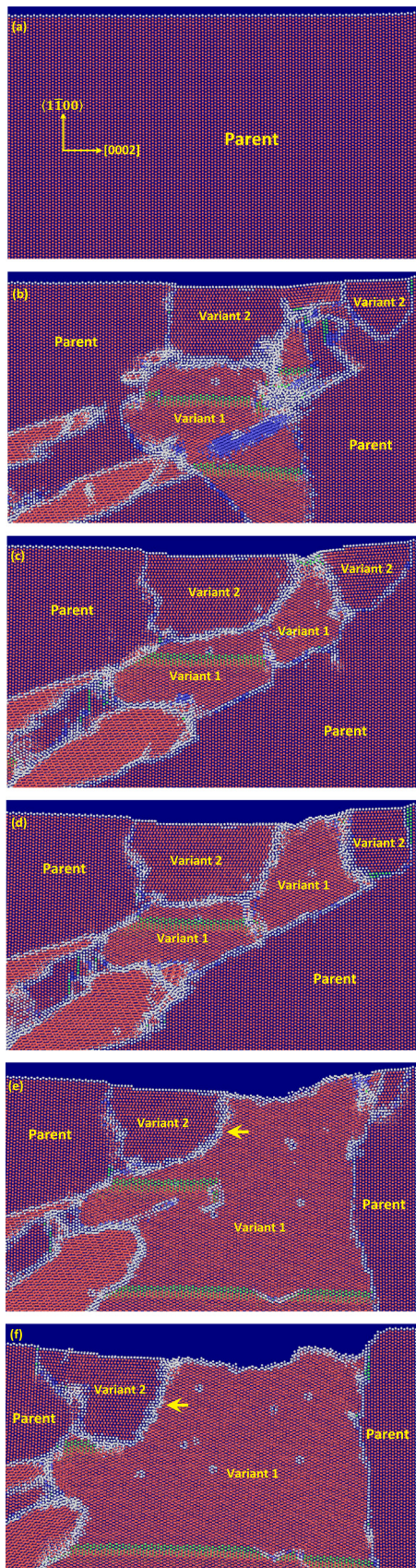


Fig. 12. Twin-twin interaction in atomistic simulations. (a) A single crystal Mg is strained in tension along the [0002]. (b) $\{10\bar{1}2\}$ twin variant 1 and 2 form. (c) Variant 1 grows into variant 2. (d) Variant 1 expands at the expense of variant 2. (e) Variant 2 in the upper right corner is almost consumed by variant 1. (f) While variant 2 grows toward the left, variant 1 further expands and consumes variant 1, as indicated by the yellow arrow.

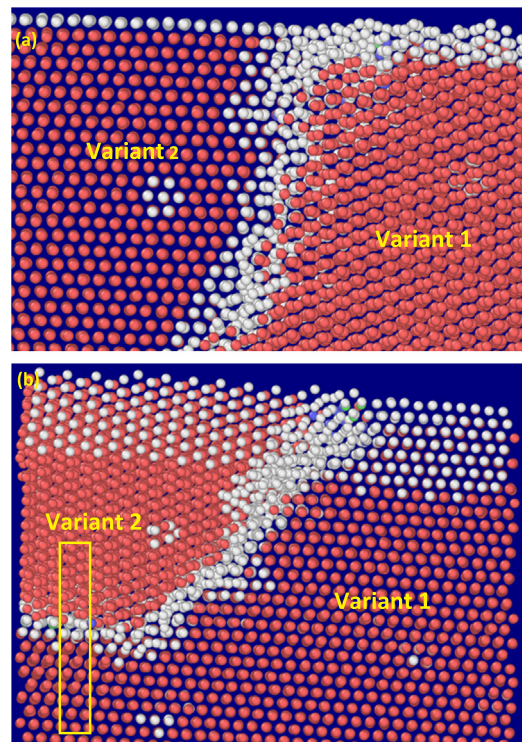


Fig. 13. Orientation relationship between variant 1 and 2. (a) A magnified view of variant 1 and 2. The basal plane of variant 2 is perpendicular to the figure plane. (b) the slice is rotated around the [0002] of the parent by $\sim 60^\circ$, such that the basal plane of variant 1 is perpendicular to the figure plane. Clearly, the boundary in Fig. 12 is a twist boundary and mobile. A side view of the boxed region is shown in Fig. 14.

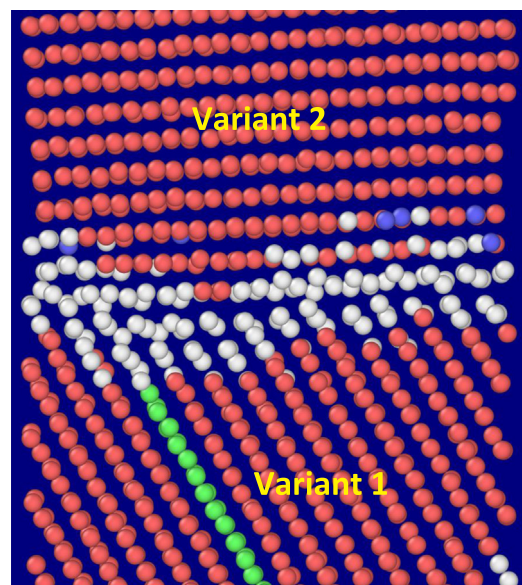


Fig. 14. Side view of the boxed region in Fig. 13. The zone axis of variant 1 and 2 can be readily identified as $\langle 1\bar{1}00 \rangle$, and the angle between the basal planes of the two variants is $\sim 60^\circ$ (or 120°).

After fracture, EBSD analysis revealed unusual lenticular domains that are neither $\{10\bar{1}2\}$ nor $\{10\bar{1}1\}$ twins. The orientation relationship satisfies $60^\circ\langle 01\bar{1}0 \rangle$ based on calculations from the Euler angles obtained in EBSD. Thus, the results obtained in this work shed new insight on the formation of the twin-like domains in specimens with large grain sizes.

The simulation results in this work (Fig. 12) show that the boundary

between two $\{10\bar{1}2\}$ primary twin variants inside a parent grain indeed has limited mobility. From the crystallography [46], if the boundary plane is parallel to $\{11\bar{2}2\}$, the orientation relationship is simply $\{11\bar{2}2\}\langle 11\bar{2}3\rangle$ twinning mode, but this twinning mode has not been observed in Mg. Most of the $60^\circ \langle 01\bar{1}0\rangle$ boundaries in our experiments and simulations are highly incoherent.

Notably, as revealed by the simulation results (Fig. 12), the limited mobility of the $60^\circ \langle 01\bar{1}0\rangle$ boundaries due to interaction between $\{10\bar{1}2\}$ primary twin variants rules out the possibility that $\{10\bar{1}2\}$ twinning is mediated by “twinning dislocations” for the following reasons. First, as shown in Figs. 3 and 6, as well as in Fig. 12, the $\{10\bar{1}2\}$ twin boundaries are rather incoherent during twin growth, consistent with numerous experimental observations [22,58] and simulations [59–61]. In Fig. 12, when two variants impinge, Variant 1 grows at the expense of Variant 2. When this occurs, a “twinning dislocation” would no longer glide on the twin boundary, instead, on an interface that the two crystals no longer satisfy the original twin relationship. However, a twinning dislocation can only glide on a specific twinning plane and lattice correspondence is uniquely defined by the twinning Burgers vector for each twinning mode [46]. Second, if two impinging variants were mediated by “twinning dislocations”, the twinning dislocations on two different twinning planes would interact to form a dislocation lock which would be immobile and thus twin boundary migration would be halted by the dislocation reaction. For one example, when a twinning Burgers vector along the $\langle 10\bar{1}\bar{1}\rangle_{\{10\bar{1}2\}}$ interacts with another twinning Burgers vector along the $\langle 01\bar{1}\bar{1}\rangle_{\{01\bar{1}2\}}$, the dislocation reaction creates a new Burgers vector of $\langle 11\bar{2}2\rangle$ which is not on either twinning planes and thus immobile. Recently, Mokdad et al. [14] studied the formation of the twin-twin boundaries by in-situ EBSD, and interesting observations consistent with ours were reported, such as a twin variant is able to grow at the expense of the other and a twin variant can branch out when interacting with the other variant. Along with many other anomalies, these observations cannot be explained by the “twinning dislocation” theories. Nevertheless, further investigations, especially in-situ experimental observations are needed to further understand the structure and mobility of this type of boundaries.

5. Conclusions

We conducted interrupted tensile tests on a rolled AZ31 Mg alloy with a relatively large grain size ($\sim 120 \mu\text{m}$) at different strain levels. The following conclusions can be drawn:

- (1) Twinning is active throughout plastic deformation until the specimens are fractured. Profuse, highly irregular $60^\circ \langle 01\bar{1}0\rangle$ inter-variant boundaries are formed as a result of interaction between different primary $\{10\bar{1}2\}$ twin variants. Although these boundaries are very close to $\{11\bar{2}2\}\langle 11\bar{2}3\rangle$ twin relationship, they are not $\{11\bar{2}2\}$ twin boundaries and are only a product of twin variants interaction.
- (2) Atomistic simulation results show that the $60^\circ \langle 01\bar{1}0\rangle$ boundaries can indeed be formed by interaction between primary twin variants. Notably, these boundaries have limited mobility as revealed in simulations. These results indicate that $\{10\bar{1}2\}$ twinning cannot be mediated by “twinning dislocations”. However, more research is needed to better understand the properties of this type of boundaries and their effect on the deformation behavior of Mg alloys.
- (3) During deformation, multiple primary $\{10\bar{1}2\}_p$ twin variants are first activated inside the parent grains. These primary twin variants grow and impinge, forming boundaries with $60^\circ \langle 01\bar{1}0\rangle$ orientation relationship. As the strain increases, secondary $\{10\bar{1}2\}_s$ twins are activated inside the primary twins. Near fracture, $\{10\bar{1}1\}_s$ secondary twins are activated inside the primary twins, followed by activation of tertiary $\{10\bar{1}2\}_t$ twins inside the $\{10\bar{1}1\}_s$ secondary twins, i.e. $\{10\bar{1}1\}-\{10\bar{1}2\}$ double twinning.

Acknowledgements

Bin Li gratefully thanks support from the U.S. National Science Foundation (NSF) (CMMI-1635088).

References

- [1] C. Cayron, Hard-sphere displacive model of extension twinning in magnesium, *Mater. Des.* 119 (2017) 361–375, <https://doi.org/10.1016/j.matdes.2017.01.047>.
- [2] M. Lentz, R.S. Coelho, B. Camin, C. Fahrenson, N. Schaefer, S. Selve, T. Link, I.J. Beyerlein, W. Reimers, In-situ, ex-situ EBSD and (HR-)TEM analyses of primary, secondary and tertiary twin development in an Mg–4wt%Li alloy, *Mater. Sci. Eng. A* 610 (2014) 54–64, <https://doi.org/10.1016/j.msea.2014.05.025>.
- [3] D. Shi, T. Liu, T. Wang, D. Hou, S. Zhao, S. Hussain, $\{10-12\}$ Twins across twin boundaries traced by in situ EBSD, *J. Alloy. Compd.* 690 (2017) 699–706, <https://doi.org/10.1016/j.jallcom.2016.08.076>.
- [4] S.R. Agnew, J.F. Nie, Preface to the viewpoint set on: the current state of magnesium alloy science and technology, *Scr. Mater.* 63 (2010) 671–673, <https://doi.org/10.1016/j.scriptamat.2010.06.029>.
- [5] S.R. Agnew, Ö. Duygulu, Plastic anisotropy and the role of non-basal slip in magnesium alloy AZ31B, *Int. J. Plast.* 21 (2005) 1161–1193, <https://doi.org/10.1016/j.ijplas.2004.05.018>.
- [6] J. Jain, W.J. Poole, C.W. Sinclair, M.A. Gharghour, Reducing the tension–compression yield asymmetry in a Mg–8Al–0.5Zn alloy via precipitation, *Scr. Mater.* 62 (2010) 301–304, <https://doi.org/10.1016/j.scriptamat.2009.11.024>.
- [7] A. Singh, H. Somekawa, T. Mukai, Compressive strength and yield asymmetry in extruded Mg–Zn–Ho alloys containing quasicrystal phase, *Scr. Mater.* 56 (2007) 935–938, <https://doi.org/10.1016/j.scriptamat.2007.02.015>.
- [8] E. Kelley, W. Hosford, Plane-strain compression of magnesium and magnesium alloy crystals, *Trans. Met. Soc. AIME* 242 (1968) 5–13.
- [9] S. Dong, Q. Yu, Y. Jiang, J. Dong, F. Wang, L. Jin, W. Ding, Characteristic cyclic plastic deformation in ZK60 magnesium alloy, *Int. J. Plast.* 91 (2017) 25–47, <https://doi.org/10.1016/j.ijplas.2017.01.005>.
- [10] P.D. Wu, X.Q. Guo, H. Qiao, S.R. Agnew, D.J. Lloyd, J.D. Embury, On the rapid hardening and exhaustion of twinning in magnesium alloy, *Acta Mater.* 122 (2017) 369–377, <https://doi.org/10.1016/j.actamat.2016.10.016>.
- [11] M.R. Barnett, Twinning and the ductility of magnesium alloys, *Mater. Sci. Eng. A* 464 (2007) 8–16, <https://doi.org/10.1016/j.msea.2007.02.109>.
- [12] B. Li, E. Ma, Zonal dislocations mediating $\{101-1\}$ $\{10-1-2\}$ twinning in magnesium, *Acta Mater.* 57 (2009) 1734–1743, <https://doi.org/10.1016/j.actamat.2008.12.016>.
- [13] Y.M. Zhu, S.W. Xu, J.F. Nie, $\{10-11\}$ Twin boundary structures in a Mg–Gd alloy, *Acta Mater.* 143 (2018) 1–12, <https://doi.org/10.1016/j.actamat.2017.09.067>.
- [14] F. Mokdad, D.L. Chen, D.Y. Li, Single and double twin nucleation, growth, and interaction in an extruded magnesium alloy, *Mater. Des.* 119 (2017) 376–396, <https://doi.org/10.1016/j.matdes.2017.01.072>.
- [15] N. Stanford, R.K.W. Marceau, M.R. Barnett, The effect of high yttrium solute concentration on the twinning behaviour of magnesium alloys, *Acta Mater.* 82 (2015) 447–456, <https://doi.org/10.1016/j.actamat.2014.09.022>.
- [16] M.R. Barnett, Z. Keshavarz, A.G. Beer, X. Ma, Non-Schmid behaviour during secondary twinning in a polycrystalline magnesium alloy, *Acta Mater.* 56 (2008) 5–15, <https://doi.org/10.1016/j.actamat.2007.08.034>.
- [17] I.J. Beyerlein, J. Wang, M.R. Barnett, C.N. Tomé, Double twinning mechanisms in magnesium alloys via dissociation of lattice dislocations, *Proc. R. Soc. A* (2012), <https://doi.org/10.1098/rspa.2011.0731> (rspa20110731).
- [18] F. Mokdad, D.L. Chen, D.Y. Li, Twin-twin interactions and contraction twin formation in an extruded magnesium alloy subjected to an alteration of compressive direction, *J. Alloy. Compd.* 737 (2018) 549–560, <https://doi.org/10.1016/j.jallcom.2017.12.043>.
- [19] Z.-Z. Shi, Y. Zhang, F. Wagner, T. Richeton, P.-A. Juan, J.-S. Lecomte, L. Capolungo, S. Berbenni, Sequential double extension twinning in a magnesium alloy: combined statistical and micromechanical analyses, *Acta Mater.* 96 (2015) 333–343, <https://doi.org/10.1016/j.actamat.2015.06.029>.
- [20] S.G. Song, G.T. Gray, Structural interpretation of the nucleation and growth of deformation twins in Zr and Ti—I. Application of the coincidence site lattice (CSL) theory to twinning problems in h.c.p. structures, *Acta Metall. Mater.* 43 (1995) 2325–2337, [https://doi.org/10.1016/0956-7151\(94\)00433-1](https://doi.org/10.1016/0956-7151(94)00433-1).
- [21] B.-Y. Liu, J. Wang, B. Li, L. Lu, X.-Y. Zhang, Z.-W. Shan, J. Li, C.-L. Jia, J. Sun, E. Ma, Twinning-like lattice reorientation without a crystallographic twinning plane, *Nat. Commun.* 5 (2014), <https://doi.org/10.1038/ncomms4297>.
- [22] X.Y. Zhang, B. Li, X.L. Wu, Y.T. Zhu, Q. Ma, Q. Liu, P.T. Wang, M.F. Horstemeyer, Twin boundaries showing very large deviations from the twinning plane, *Scr. Mater.* 67 (2012) 862–865, <https://doi.org/10.1016/j.scriptamat.2012.08.012>.
- [23] M.D. Nave, M.R. Barnett, Microstructures and textures of pure magnesium deformed in plane-strain compression, *Scr. Mater.* 51 (2004) 881–885, <https://doi.org/10.1016/j.scriptamat.2004.07.002>.
- [24] Q. Yu, J. Wang, Y. Jiang, R.J. McCabe, C.N. Tomé, Co-zone $10-12$ twin interaction in magnesium single crystal, *Mater. Res. Lett.* 2 (2014) 82–88, <https://doi.org/10.1080/21663831.2013.867291>.
- [25] Q. Yu, J. Wang, Y. Jiang, R.J. McCabe, N. Li, C.N. Tomé, Twin–twin interactions in magnesium, *Acta Mater.* 77 (2014) 28–42, <https://doi.org/10.1016/j.actamat.2014.05.030>.
- [26] H. El Kadiri, J. Kapil, A.L. Oppedal, L.G. Hector, S.R. Agnew, M. Cherkaoui, S.C. Vogel, The effect of twin–twin interactions on the nucleation and propagation

- of {10-12} twinning in magnesium, *Acta Mater.* 61 (2013) 3549–3563, <https://doi.org/10.1016/j.actamat.2013.02.030>.
- [27] B.M. Morrow, E.K. Cerreta, R.J. McCabe, C.N. Tomé, Toward understanding twin–twin interactions in hcp metals: utilizing multiscale techniques to characterize deformation mechanisms in magnesium, *Mater. Sci. Eng. A* 613 (2014) 365–371, <https://doi.org/10.1016/j.msea.2014.06.062>.
- [28] C. Cayron, R. Logé, Evidence of new twinning modes in magnesium questioning the shear paradigm, *J. Appl. Crystallogr.* 51 (2018) 809–817, <https://doi.org/10.1107/S1600576718005678>.
- [29] H. Chen, T. Liu, S. Xiang, Y. Liang, Abnormal migration of twin boundaries in rolled AZ31 alloy containing intersecting {10-12} extension twins, *J. Alloy. Compd.* 690 (2017) 376–380, <https://doi.org/10.1016/j.jallcom.2016.08.154>.
- [30] Q. Ma, H. El Kadiri, A.L. Oppedal, J.C. Baird, B. Li, M.F. Horstemeyer, S.C. Vogel, Twinning effects in a rod-textured AM30 magnesium alloy, *Int. J. Plast.* 29 (2012) 60–76, <https://doi.org/10.1016/j.ijplas.2011.08.001>.
- [31] A. Ostapovets, J. Buršík, K. Krahula, L. Král, A. Serra, On the relationship between and conjugate twins and double extension twins in rolled pure Mg, *Philos. Mag.* 97 (2017) 1088–1101, <https://doi.org/10.1080/14786435.2017.1290846>.
- [32] D. Shi, T. Liu, D. Hou, H. Chen, F. Pan, H. Chen, The effect of twin–twin interaction in Mg3Al1Zn alloy during compression, *J. Alloy. Compd.* 685 (2016) 428–435, <https://doi.org/10.1016/j.jallcom.2016.05.338>.
- [33] B.-C. Suh, J.H. Kim, J.H. Hwang, M.-S. Shim, N.J. Kim, Twinning-mediated formability in Mg alloys, *Sci. Rep.* 6 (2016) srep22364, <https://doi.org/10.1038/srep22364>.
- [34] S.-G. Hong, S.H. Park, C.S. Lee, Strain path dependence of {10–12} twinning activity in a polycrystalline magnesium alloy, *Scr. Mater.* 64 (2011) 145–148, <https://doi.org/10.1016/j.scriptamat.2010.09.030>.
- [35] A. Serra, D.J. Bacon, Modelling the motion of {11-22} twinning dislocations in the HCP metals, *Mater. Sci. Eng. A* 400–401 (2005) 496–498, <https://doi.org/10.1016/j.msea.2005.01.067>.
- [36] B. Li, H.E. Kadiri, M.F. Horstemeyer, Extended zonal dislocations mediating twinning in titanium, *Philos. Mag.* 92 (2012) 1006–1022, <https://doi.org/10.1080/14786435.2011.637985>.
- [37] Y. Guo, H. Abdolvand, T.B. Britton, A.J. Wilkinson, Growth of {11-22} twins in titanium: a combined experimental and modelling investigation of the local state of deformation, *Acta Mater.* 126 (2017) 221–235, <https://doi.org/10.1016/j.actamat.2016.12.066>.
- [38] M.S. Daw, M.I. Baskes, Semiempirical, quantum mechanical calculation of hydrogen embrittlement in metals, *Phys. Rev. Lett.* 50 (1983) 1285–1288, <https://doi.org/10.1103/PhysRevLett.50.1285>.
- [39] M.S. Daw, M.I. Baskes, Embedded-atom method: derivation and application to impurities, surfaces, and other defects in metals, *Phys. Rev. B* 29 (1984) 6443–6453, <https://doi.org/10.1103/PhysRevB.29.6443>.
- [40] X.-Y. Liu, J.B. Adams, F. Ercolessi, J.A. Moriarty, EAM potential for magnesium from quantum mechanical forces, *Model. Simul. Mater. Sci. Eng.* 4 (1996) 293, <https://doi.org/10.1088/0965-0393/4/3/004>.
- [41] X. Liu, J. Wang, Low-energy, mobile grain boundaries in magnesium, *Sci. Rep.* 6 (2016) srep21393, <https://doi.org/10.1038/srep21393>.
- [42] P. Chen, B. Li, D. Culbertson, Y. Jiang, Contribution of extension twinning to plastic strain at low stress stage deformation of a Mg-3Al-1Zn alloy, *Mater. Sci. Eng. A* 709 (2018) 40–45, <https://doi.org/10.1016/j.msea.2017.10.038>.
- [43] J.D. Honeycutt, H.C. Andersen, Molecular dynamics study of melting and freezing of small Lennard-Jones clusters, *J. Phys. Chem.* 91 (1987) 4950–4963, <https://doi.org/10.1021/j100303a014>.
- [44] A. Stukowski, Visualization and analysis of atomistic simulation data with OVITO—the open visualization tool, *Model. Simul. Mater. Sci. Eng.* 18 (2010) 015012, <https://doi.org/10.1088/0965-0393/18/1/015012>.
- [45] B. Li, X.Y. Zhang, Twinning with zero twinning shear, *Scr. Mater.* 125 (2016) 73–79, <https://doi.org/10.1016/j.scriptamat.2016.07.004>.
- [46] J.W. Christian, S. Mahajan, Deformation twinning, *Prog. Mater. Sci.* 39 (1995) 1–157.
- [47] C.D. Barrett, H. El Kadiri, M.A. Tschopp, Breakdown of the Schmid law in homogeneous and heterogeneous nucleation events of slip and twinning in magnesium, *J. Mech. Phys. Solids* 60 (2012) 2084–2099, <https://doi.org/10.1016/j.jmps.2012.06.015>.
- [48] S. Mu, J.J. Jonas, G. Gottstein, Variant selection of primary, secondary and tertiary twins in a deformed Mg alloy, *Acta Mater.* 60 (2012) 2043–2053, <https://doi.org/10.1016/j.actamat.2012.01.014>.
- [49] S.R. Agnew, C.N. Tomé, D.W. Brown, T.M. Holden, S.C. Vogel, Study of slip mechanisms in a magnesium alloy by neutron diffraction and modeling, *Scr. Mater.* 48 (2003) 1003–1008, [https://doi.org/10.1016/S1359-6462\(02\)00591-2](https://doi.org/10.1016/S1359-6462(02)00591-2).
- [50] A. Serra, D.J. Bacon, R.C. Pond, Twins as barriers to basal slip in hexagonal-close-packed metals, *Metall. Mater. Trans. A* 33 (2002) 809–812, <https://doi.org/10.1007/s11661-002-0149-7>.
- [51] H. El Kadiri, A.L. Oppedal, A crystal plasticity theory for latent hardening by glide twinning through dislocation transmutation and twin accommodation effects, *J. Mech. Phys. Solids* 58 (2010) 613–624, <https://doi.org/10.1016/j.jmps.2009.12.004>.
- [52] X.Y. Lou, M. Li, R.K. Boger, S.R. Agnew, R.H. Wagoner, Hardening evolution of AZ31B Mg sheet, *Int. J. Plast.* 23 (2007) 44–86, <https://doi.org/10.1016/j.ijplas.2006.03.005>.
- [53] P. Chen, B. Li, D. Culbertson, Y. Jiang, Negligible effect of twin-slip interaction on hardening in deformation of a Mg-3Al-1Zn alloy, *Mater. Sci. Eng. A* 729 (2018) 285–293, <https://doi.org/10.1016/j.msea.2018.05.067>.
- [54] M.Z. Bian, K.S. Shin, {10-12} twinning behavior in magnesium single crystal, *Met. Mater. Int.* 19 (2013) 999–1004, <https://doi.org/10.1007/s12540-013-5012-4>.
- [55] J. Jain, J. Zou, C.W. Sinclair, W.J. Poole, Double tensile twinning in a Mg–8Al–0.5Zn alloy, *J. Microsc.* 242 (2011) 26–36, <https://doi.org/10.1111/j.1365-2818.2010.03434.x>.
- [56] A. Chakkeedath, C.J. Boehlert, In situ scanning electron microscopy observations of contraction twinning and double twinning in extruded Mg-1Mn (wt%), *JOM* 67 (2015) 1748–1760, <https://doi.org/10.1007/s11837-015-1478-5>.
- [57] B. Li, Q. Ma, Z. McClelland, S.J. Horstemeyer, W.R. Whittington, S. Brauer, P.G. Allison, Twin-like domains and fracture in deformed magnesium, *Scr. Mater.* 69 (2013) 493–496, <https://doi.org/10.1016/j.scriptamat.2013.06.014>.
- [58] Q. Ma, B. Li, E.B. Marin, S.J. Horstemeyer, Twinning-induced dynamic recrystallization in a magnesium alloy extruded at 450 °C, *Scr. Mater.* 65 (2011) 823–826, <https://doi.org/10.1016/j.scriptamat.2011.07.046>.
- [59] J.P. Simon, Computer simulation of twin boundaries in HCP normal metals: Li, Be, Mg, Zn, Cd, *J. Phys. F Met. Phys.* 10 (1980) 337, <https://doi.org/10.1088/0305-4608/10/3/004>.
- [60] B. Li, E. Ma, Atomic shuffling dominated mechanism for deformation twinning in magnesium, *Phys. Rev. Lett.* 103 (2009) 035503, <https://doi.org/10.1103/PhysRevLett.103.035503>.
- [61] B. Dutta, J. Neugebauer, M. Friák, S. Sandlöbes, T. Hickel, X. Zhang, Z. Pei, Atomic structures of twin boundaries in hexagonal close-packed metallic crystals with particular focus on Mg, *NPJ Comput. Mater.* 3 (2017) 6, <https://doi.org/10.1038/s41524-017-0010-6>.